Energy Advances

ROYAL SOCIETY OF CHEMISTRY

PAPER

View Article Online
View Journal | View Issue

Cite this: *Energy Adv.*, 2024, 3, 1965

Zinc oxide nanoflake/reduced graphene oxide nanocomposite-based dual-acting electrodes for solar-assisted supercapacitor applications†

Cigdem Tuc Altaf, [a] Tuluhan Olcayto Colak,[b] Arpad Mihai Rostas, [c] Crina Socaci, [c] Mihaela Diana Lazar, [c] Lucian Barbu Tudoran,[c] Mohamad Hasan Aleinawi, [d] Feray Bakan Misirlioglu,[e] Ipek Deniz Yildirim,[d] Emre Erdem,[d] Nurdan Demirci Sankir *[ab] and Mehmet Sankir *[ab]

Received 19th April 2024,
Accepted 19th June 2024

DOI: 10.1039/d4ya00253a

rsc.li/energy-advances

There is an ever-growing requirement for systems that enable both conversion and storage of solar energy in the same device, thereby reducing the need for grid electricity and fossil fuels. Although photo-supercapacitors (PSCs) potentially meet this requirement, it is essential to develop high-performance devices in which conversion and storage can be achieved on the same electrode. This study investigated two-electrode PSC systems based on three-dimensional (3D) zinc oxide (ZnO) nanoflakes/reduced graphene oxide (rGO) nanocomposites to meet the need for *in situ* solar energy conversion/storage. To better understand the effect of rGO and 3D ZnO nanoflakes separately, three different compositions have been studied, in which the weight percent of rGO changes from 8 to 32%. The energy density increases as the amount of rGO increases, but the composite material loses its light sensitivity above a critical value. Therefore, the electrodes containing 16% rGO exhibited higher performance than those containing 32% and 8% rGO. As a result, the (16%) rGO/ZnO-based PSC exhibited superior performance compared to the other samples, with its ability to maintain 100% of its performance at 40 000 cycles, its areal capacitance of 40 mF cm^{-2} and energy density values of 22 μW h cm^{-2}, which were 170% higher than under dark condition measurements.

Introduction

Efforts to limit or even stop the use of fossil fuels are accelerating due to the serious problems caused by them, like global warming. Therefore, the importance of innovative technologies using renewable energy sources is increasing daily.[1–5] Among innovative technologies, systems that enable solar energy conversion into storable forms have great potential.[6–10] Although hydrogen obtained by water splitting using photoelectrochemical or photo-catalytic routes provides significant advantages in this field, problems related to the storage of converted solar energy are still challenging.[11–14] Besides, the progress in renewable energy systems to overcome environmental problems and the rising prevalence of electronics in daily life have impelled scientific researchers to build up a new generation – systems that combine solar energy conversion and storage in a single and compact device, named photo-supercapacitors (PSCs).[15–24] The combined solar conversion and storage systems, consisting of solar cells and supercapacitor units, are the most reported PSC devices.[25–29] On the other hand, dual-acting electrodes enable solar energy conversion and storage on the same electrode. Using these electrodes in a single device would provide a compact, cheap, and efficient PSC system.[17]

Zinc oxide (ZnO) is a widely utilized semiconductor material with a wide band-gap value (~3.2 eV) and tuneable electrical and optoelectronic properties. Thus, ZnO nanostructures are promising for many energy conversion/storage applications by controlling the synthesis conditions.[30–32] In addition to its suitability in pseudo-capacitor applications due to high electrochemical activity,[32] recent research works confirmed that the ZnO nanostructures have also become very attractive for PSC applications that require high optical absorption.[33,34] In recent studies, we demonstrated that zinc oxide (ZnO) nanowire and nanoflower morphologies showed synergistic properties with

[a] *Department of Materials Science and Nanotechnology Engineering, TOBB University of Economics and Technology, Sogutozu Caddesi No. 43, Sogutozu 06560, Ankara, Turkey. E-mail: nsankir@etu.edu.tr, msankir@etu.edu.tr*
[b] *Micro and Nanotechnology Graduate Program, TOBB University of Economics and Technology, Sogutozu Caddesi No. 43, Sogutozu 06560, Ankara, Turkey*
[c] *National Institute for Research and Development of Isotopic and Molecular Technologies – INCDTIM, 67-103 Donat, 400293 Cluj-Napoca, Romania*
[d] *Faculty of Engineering and Natural Sciences, Sabanci University, Orhanli, Tuzla, 34956, Istanbul, Turkey*
[e] *Sabanci University Nanotechnology Research and Application Center, 34956, Istanbul, Turkey*

† Electronic supplementary information (ESI) available. See DOI: https://doi.org/10.1039/d4ya00253a

2D carbon-based materials such as MXene, graphitic carbon nitride (g-C_3N_4), graphene oxide (GO), and reduced-graphene oxide (rGO) materials for dual-acting electrodes for PSC applications.[34–39] In our previous study, we confirmed that 1D ZnO nanoparticles combined with the 2D GO and rGO electrodes served as both pseudo-capacitive and photoactive electrodes, in which the outstanding optical properties of ZnO were combined with 2D materials having unique electrical and electrochemical properties.[39] It is known that morphological and structural changes in ZnO thin films lead to electrochemical, catalytic, and optical performance manipulation.[40–43] Herein, we established PSC devices based on nanocomposites of rGO material with 3D ZnO nanoflakes, which are superior to 1D ZnO in terms of effective surface area and light absorption capacity since the morphology of ZnO plays a very important role in physical and electrochemical performance, such as defect density and centers, charge transport, and optical absorption, which directly affect the electrochemical energy storage performance. Thus, the present work on a property/performance relationship by synthesizing 3D ZnO nanoflake/rGO composites to investigate the effect of the physical properties changing with the morphology of the 3D ZnO nanostructures on the PSC performance would be a reputable contribution to the literature.

Another outstanding advantage of ZnO is that optoelectrical and electrochemical properties can be tailored by controlling the defect's nature.[44] Defects occurring within the structure, such as vacancies or interstitial atoms, can cause lattice distortion and differences in the material's electrochemical, electrical, and chemical properties. In addition, defects can accelerate the ionic transfer by providing active sites in the structure. Since defect structures generally act as electron traps, they play a role in reducing electrical conductivity and thus decreasing device performance, but the presence of defect structures can be advantageous, especially in terms of photocatalytic and electrochemical properties.[45] From the perspective of electrochemical energy storage, defects can improve the device's performance by promoting ion diffusion and electron transfer and providing extra electroactive sites.[46] Previously, W. Zhou *et al.* reported that oxygen-deficient ZnO/CoO nanowire heterojunctions presented a specific capacity of 845 C g^{-1}, enhancing the electrochemical performance.[47] They concluded that the oxygen vacancies in the structure improved the electrochemical performance by shortening the distance of electrons along the conduction band and promoting the redox reaction.[47] S. Kasap *et al.* reported that the defective structure of ZnO improved the electrochemical performance due to the reduced specific resistivity.[48] Similarly, carbonaceous materials like graphene oxide are highly defective. Defects such as dangling bonds and C-radicals in these materials are important for their physical and chemical properties.[49,50] Additionally, ZnO structures composited with graphene oxide are preferred, especially in energy conversion and storage areas.[51,52] In the literature, both ZnO and graphene oxide have been used separately for PSC applications.[33,53–55] D. Solis-Cortes *et al.* reported Ag_2S quantum dot decorated ZnO nanorod array electrodes for PSCs, in which PEDOT was used as a charge storage counter electrode.[33] They showed that the specific capacitance and storage efficiency of this device were 0.667 mF cm^{-2} and 6.83%, respectively.[33] A. Roy *et al.* reported a photoelectrochemical-type supercapacitor based on a $BiVO_4$–RGO bilayer photocapacitive electrode.[55] They concluded that the $BiVO_4$–RGO electrode displays typical EDLC behavior and provides good performance as a supercapacitor exhibiting a specific capacitance of 141.8 F g^{-1} measured at a current density of 0.2 A g^{-1}.[55] However, there is a very limited number of such studies in the literature, and there is a great need to examine the performances of rGO and ZnO nanocomposites in PSC applications based on morphology and structural properties.

Within the framework of all this motivation, in this study, our group aimed to control the defect structures by combining a ZnO morphology, which has not been studied before in photo-supercapacitor applications, with nanoflakes and rGO, thus improving the photoelectrochemical charge storage performance. In this direction, we prepared composites with three different ZnO/rGO ratios and focused on the property/performance relationships of these materials. We aim to provide innovative solutions for systems that can be charged directly by sunlight and thus meet their power needs. With this study, we offer innovative and efficient solutions for autonomous systems, whose popularity and usage area have increased in recent years.

Materials and methods

Reagents

Zinc acetate dihydrate ($Zn(CH_3COO)_2{\cdot}2H_2O$, Sigma Aldrich, 98%), urea (CH_4N_2O, ACS reagent, 99.0–100.5%), polyvinyl alcohol (PVA, Sigma-Aldrich-87–90% hydrolyzed), lithium chloride (LiCl, ACS reagent), dimethyl formamide (DMF, Sigma-Aldrich), ethanol (C_2H_5OH, Sigma-Aldrich), and fluorine-doped tin oxide-coated glass (FTO, resistivity 10 Ω cm^2) were purchased from Sigma-Aldrich.

Synthesis of the photoactive composite materials

The reduced graphene oxide (rGO) was prepared by thermal reduction of GO, as described in our previous work.[39] 3D ZnO nanoflakes were synthesized from zinc acetate dihydrate ($Zn(CH_3COO)_2{\cdot}2H_2O$) and urea in ethanol *via* hydrothermal reaction at 180 °C for 14 h. Briefly, 50.0 mM $Zn(CH_3COO)_2{\cdot}2H_2O$ and 100 mM urea were dissolved in 60.0 mL ethanol by stirring for 30 min. The solution was transferred to a Teflon-lined stainless steel autoclave for the reaction. After cooling to room temperature, the product was separated by centrifugation, dried at 60 °C, and then calcinated at 300 °C for 30 min. The rGO/3D ZnO nanoflake composite material was prepared in dimethyl formamide (DMF) by a hydrothermal method. Before synthesis, 10 mg of rGO powder was sonicated in DMF for 1 h to obtain a good dispersion before adding 50 mg of ZnO nanoflakes for 16% (wt%) rGO/ZnO. Then, the mixture was sonicated for an additional 1 h and reacted at 100 °C for 3 h. The composite powder was centrifuged at 2000 rpm for 15 min and dried at 90 °C overnight. The other rGO/ZnO nanoflake composites were prepared by altering rGO amount (8 and 32%).

Characterization

UV-vis optical transmission (T%) and reflectance (R%) measurements of the thin films prepared by dropping cations of the composite ink were performed on a PerkinElmer, Lambda 650 S, from 700 to 300 nm. The absorption value was calculated using both %T and %R. Photoluminescence (PL) spectra were acquired with an Edinburgh instrument spectrofluorometer FS5 at room temperature with an excitation wavelength of 240 nm. Scanning and transmission electron microscopy (SEM-TEM) was carried out on a Hitachi HD-2700 STEM microscope (Hitachi, Japan) operating at 200 kV. Before the analysis, each sample was finely ground and dispersed in ethanol by sonication. X-ray diffraction spectroscopy analysis was performed using a PANalytical/Philips X'Pert MRD system. Electron paramagnetic resonance (EPR) spectroscopy was performed on a continuous wave dual band X- and Q-band spectrometer Bruker ELEXSYS E500. The X-band measurements were performed at 9.87 GHz with an X-SHQ 4119HS-W1 Bruker microwave cavity, while an ER 5106 QT standard Bruker cavity operating at 34 GHz was employed for the Q-band measurements. All EPR measurements were carried out at room temperature.

PSC device assembly and photo(electrochemical) tests

The synthesized composite products were dispersed in an alcohol mixture (methanol/isopropanol/1-butanol) by sonicating for 2 h. The dispersion of the product has been coated on the commercial fluorine-doped tin oxide (FTO) coated glass substrates *via* drop casting by loading 10 mg of active material. PVA–LiCl electrolyte was prepared by dissolving 3 g of PVA in 30 mL of deionized water and heated to 85 °C to obtain a homogenous solution. 3 g of LiCl was added to the solution and stirred at 85 °C for 1 h. The working photoactive electrode, standard filter paper, carbon paper, and bare FTO were wetted with PVA–LiCl solution and assembled in the given order.

The photo(electro) chemical performance evaluations of the PSC devices prepared from nanocomposite materials have been investigated by electrochemical characterization methods such as cyclic voltammetry (CV), galvanostatic charge/discharge (GCD), and open circuit potential (V_{OC}) using a Gamry potentiostat/galvanostat workstation in the dark and under UV illumination. A radiation source (8.8 mW cm^{-2}) provided a UV-illuminated environment for the photoelectrochemical measurements. Fundamental parameters for the efficiency of

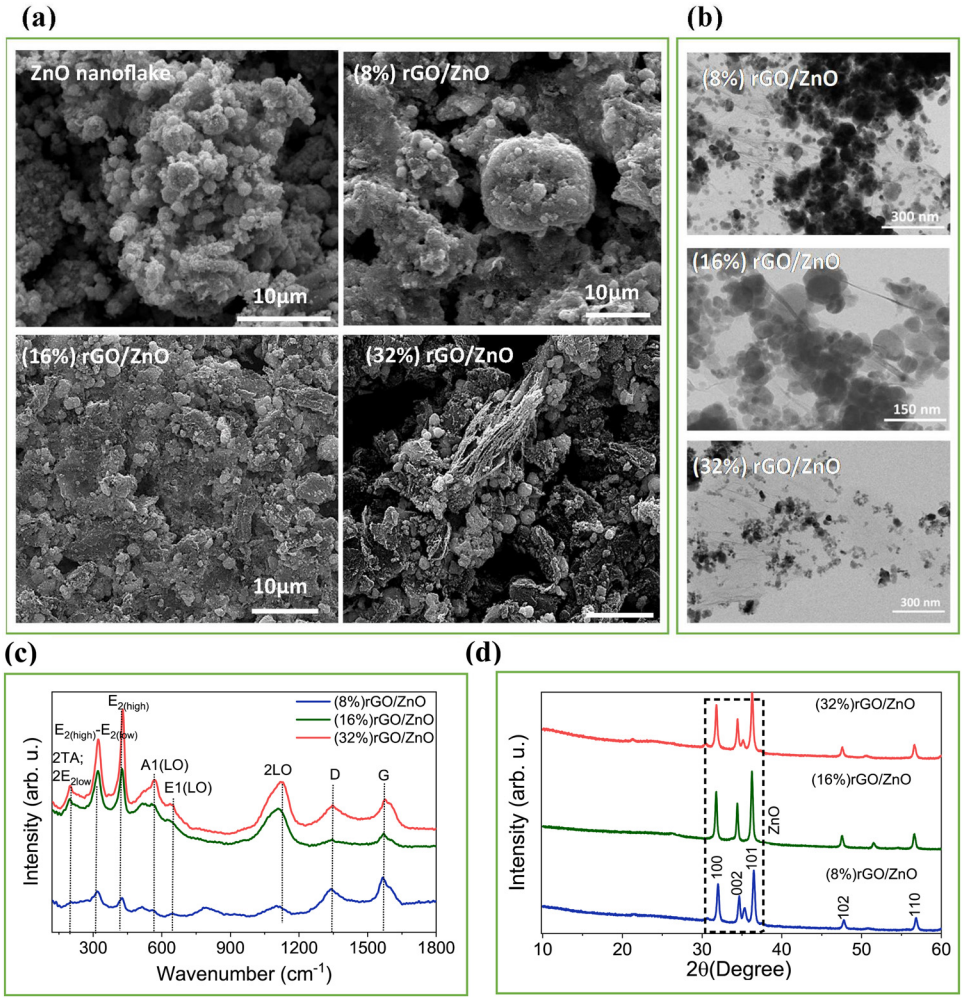

Fig. 1 (a) SEM and (b) TEM images of the synthesized powder products. (c) Raman and, (d) XRD spectra of the synthesized composite materials.

supercapacitor devices such as Coulombic efficiency (%), areal capacitance (C_p, mF cm^{-2}), areal energy density (E, μW h cm^{-2}), and areal power density (P, mW cm^{-2}) have been evaluated using the equations given in the ESI.† The electrochemical impedance spectroscopy (EIS) measurements have been performed at the potential of 0 V over the frequency range from 1 MHz to 0.1 Hz using a Gamry workstation under dark and UV light conditions.

Results and discussion

The morphology and microstructure of the rGO/3D ZnO nanoflake composite materials and the pristine 3D ZnO nanoflake were examined by SEM analysis (Fig. 1(a)), confirming the pristine ZnO and the agglomerated spherical particle formation (Fig. S1a, ESI†), possibly due to the high surface energy of the nanoparticles.[56] On the other hand, increasing the rGO ratio in the composite shows the lamellar structure of rGO (32%) in the rGO/3D ZnO composite material (Fig. S1b, ESI†). TEM images presented in Fig. 1(b) show an agglomerated composite in which ZnO particles appear surrounded by rGO sheets. However, increasing the rGO ratio results in less agglomeration as it causes dispersion media for ZnO nanoparticles.

Fig. 1(c) illustrates the Raman spectra of three rGO/3D ZnO nanostructures, showcasing variations corresponding to different rGO/3D ZnO weight ratios. ZnO is characterized by the predominance of E_2 modes in standard backscattering experiments, which serve as a distinctive Raman fingerprint.[57] A distinct peak was observed at 428 cm^{-1}, representing the characteristic Wurtzite E_2(high) mode for ZnO. This peak shifts towards lower wavelengths with higher concentrations of rGO, possibly due to spatial variances in strain leading to an anisotropic response in ZnO.[35] Another notable vibration at 321 cm^{-1} is commonly associated with the second-order Raman process, specifically the E_2(high)–E_2(low) difference mode. Symmetry considerations and intensity analysis dependent on temperature support this assignment.[57,58] The spectra also exhibit relatively weak and broad bands around 567 cm^{-1}, indicating the A_1(LO) phonon mode, which arises when the c-axis of wurtzite ZnO aligns parallel to the sample surface. Significant second-order characteristics can be deduced from LO overtones and combinations of LO modes in the high-frequency range. Broadband around 1120 cm^{-1} may correspond to 2LO scattering from flat bands along the A–L–M line.[57] This peak might be combined with the modes $2A_1$(LO) and $2E_1$(LO) at the Γ symmetry point of the Brillouin zone. Regarding the presence of rGO in the structure, peaks observed at approximately 1340 cm^{-1} and 1570 cm^{-1} represent the D and G bands, respectively.[39,58] The D band is generated by transverse optical phonons near the K corner of the first Brillouin zone, which stem from the breathing modes of the six-atom rings in graphene. Activation of this mode

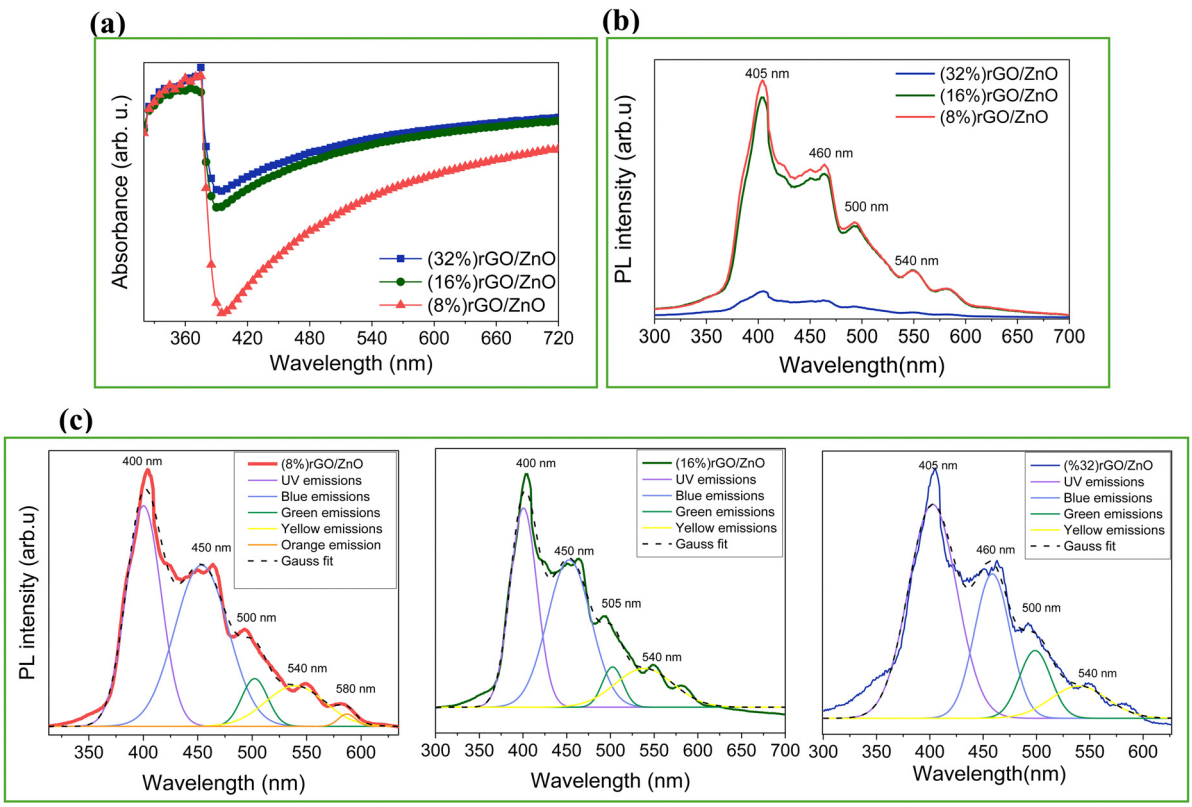

Fig. 2 (a) UV-vis spectra, (b) comparative PL emission spectra, and (c) PL peak deconvolution results of the rGO/3D ZnO nanostructures with 8, 16, and 32% of rGO content.

indicates a structural defect. Conversely, the G band results from first-order Raman scattering by in-plane optical transverse and longitudinal phonons at the Brillouin zone center.[58]

XRD patterns of the synthesized rGO/3D ZnO nanocomposites are shown in Fig. 1(d). The signals belonging to ZnO nanoflakes were residing at 2θ = 31.90, 34.52, 36.31, 47.75, and 56.85° corresponding to the crystallographic planes (100), (002), (101), (102), and (110), respectively. The diffraction pattern signifies that the ZnO nanoparticles are in the form of a hexagonal wurtzite crystal structure (PDF #36–1451). The diffraction peak, which was supposed to be observed at 26.9° for the (002) planes of rGO, was not observed due to the low rGO content in the composites, which was buried under the high diffraction intensity of ZnO peaks, similar to the previously reported work, due to the suppressing of the sharp peaks belonging to highly crystalline ZnO nanoflakes.

UV-vis absorption spectra of the nanocomposite materials were collected from the thin film photoelectrodes deposited by the composite suspension. Fig. 2(a) shows that all samples present strong absorption characteristics at ~400 nm. The absorption edge of the rGO/3D ZnO composites stays the same as the pristine ZnO (as given in Fig. S1c, ESI†), indicating that the band gap values remain very similar with increasing rGO amount.[59] Also, it was observed that the absorption in the visible region enhanced with rGO addition (Fig. S1c, ESI†), and increasing rGO content increased the absorption in the visible region.[60] Fig. 2(b) below shows the photoluminescence (PL) spectra, where a major increase in the peak intensities can be observed for the 16% and 8% rGO-containing samples compared to the 32%, indicating an increase in the optical activity of the composite materials. The lower intensities in the 32% samples can be attributed to the quenching effect of rGO on ZnO.[61] A major decrease in UV emissions and an increase in blue emissions by varying the composite ratio can be attributed to anchoring the rGO sheets on the ZnO surface.[35] Further analysis by Gaussian fitting of the PL spectra for the samples with 8, 16, and 32% rGO contents are shown in Fig. 2(c) and Table S1 (ESI†) associated with radiative peaks in the UV and visible region at 400 and 450, 500, 540, and 580 nm, respectively. These emissions correspond to near-band emissions arising from electron–hole recombination. The major PL signal observed in the UV region (400 nm) is accredited to near-band edge excitonic emission. Additional deep-level emissions occur by different intrinsic defects in ZnO, such as oxygen vacancy (V_O), zinc vacancy (V_{Zn}), interstitial zinc (Zn_i), interstitial oxygen (O_i), and antisite oxygen (O_{Zn}) from the hydrothermal synthesis of nanostructured ZnO in several literature works.[62–64]

EPR spectroscopy was employed to analyze the defect centers present in the precursor ZnO material and the rGO/3D ZnO composites (Fig. 3). The X-band EPR spectrum of the pristine ZnO (Fig. 3a) is composed of two broad signals with different *g*-values, 2.0035 and 1.9620, that correspond to shell and core defects, respectively in the ZnO material, as is already reported in the literature.[65] Based on the core–shell model,[44] paramagnetically active intrinsic defect centers have *g*-factors at $g \sim 2.0$ located at the surface, whereas the defects located in the lattice (volume) are core defects. Therefore, with this model's help, it is possible to distinguish the local accommodation and the electronic environment of defects. Further EPR analysis at a higher magnetic field in the Q-band (see Fig. S2, ESI†) of the pristine ZnO reveals the presence of a more complex EPR signal composed of four different resonances. The resonances with g = 2.015 and 1.980 are due to singly ionized oxygen vacancies on the surfaces of the material, causing the blue emission observed in the PL measurements. In this context, nanoflake morphology refers to a structure with a two-dimensional, flat, and thin geometry at the nanoscale. This is distinct from structures like nanowires, which are elongated and wire-like, and nanoparticles, which are three-dimensional particles with a roughly spherical or irregular shape. The peculiarity of nanoflakes lies in their high surface area-to-volume ratio due to their thin, planar shape. This can make them highly defective at the surface, which is confirmed here *via* EPR by enhancing the signal $g \sim 2$ region. In contrast, previous studies on nanowires[66] and nanoparticles[67] revealed much fewer surface defect states than the present study. Besides, the ZnO-related EPR signals start to vanish by increasing the rGO content,

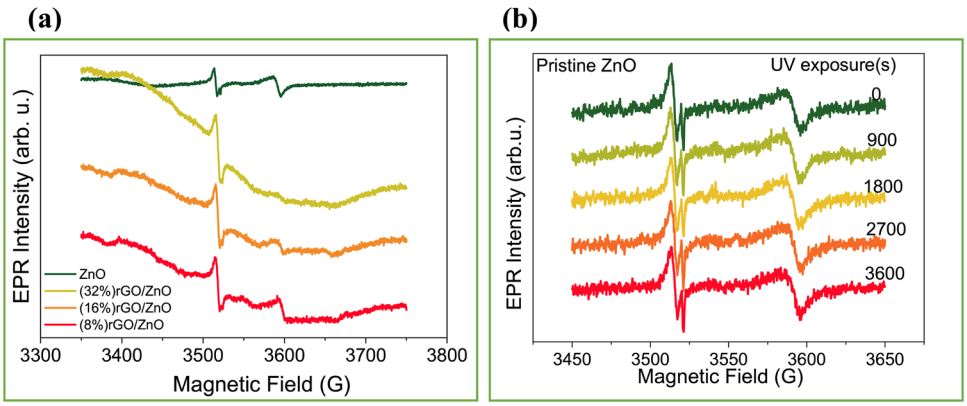

Fig. 3 EPR spectra of the ZnO nanoflake and rGO/3D ZnO nanostructures (a), and 3D ZnO nanoflake EPR signal evolution under UV irradiation for 0–3600 seconds (b).

indicating that the defect centers present in the pristine ZnO material play a key role in forming the composite materials. As presented in earlier studies on ZnO materials with different morphologies, irradiating it with UV light generates electron–hole pairs in the material, while the EPR signal increases with the irradiation.[34] Fig. 3b and Fig. S2 and S3 (ESI†) present the results after irradiating the pristine and the composite rGO/3D ZnO materials with UV light for 1 h. The EPR signal intensities do not change during irradiation, indicating that the recombination time of the photogenerated electron–hole pairs is very fast. EPR analysis results for the composite powders under UV irradiation are given in Fig. S3 (ESI†).

The prepared PSC devices were (photo) electrochemically analyzed with electrochemical tests under UV irradiation and in the dark. The CV measurements were taken at a 1.1 V potential window, and the results are summarized in Fig. 4(a)–(e) and Fig. S4(a)–(c) (ESI†). Fig. 4(a)–(c) displays the CV scans at the scan rates between 5 and 100 mV s^{-1} for the PSC devices prepared by (8%) rGO, (16%) rGO, and (32%) rGO incorporation, respectively. It was observed that the increasing rGO amount increases the area of the CV curves due to the enhancement in the ionic and electronic conductivities.[60] Also, increasing the rGO amount resulted in a quasi-rectangular-shaped hysteresis loop with no redox peaks due to the pseudocapacitive performance and a large gathering in electronic charge.[60] Thus, (16%) rGO and (32%) rGO in the composite resulted in enhanced C_A values in the dark (Fig. S4d, ESI†). As we compare the dark and UV-illuminated CV profile for each composite ratio, the best result was observed for the (16%) rGO/3D ZnO-based PSC with a C_A value of 34.5 mF cm^{-2} at a 5 mV s^{-1} scan rate (Fig. S4(e), ESI†). The open circuit potential (V_{OC}) of each PSC device collected under UV on/off conditions is given in Fig. 4(f), indicating that the best response belongs to the (16%) rGO/ZnO-based PSC.

GCD curves of the PSC devices under UV illumination (Fig. 5(a)–(c)) and under dark conditions (Fig. S5, ESI†) for various current densities have been investigated. The (16%)- and (32%) rGO/3D ZnO PSC devices could be charged up to 2.0 V potential, while the PSC device with the least amount of rGO ((8%) rGO/3D ZnO) could be charged up to 1.5 V, due to the lower electronic conductivity of ZnO. The energy densities of rGO/3D ZnO nanocomposites under dark and UV illumination conditions are given in Fig. 5(d) and (e). The maximum energy density of 23 μA h cm^{-2} at 0.4 mA cm^{-2} has been calculated for (16%) rGO/3D ZnO under UV illumination and at 2.0 V. Since the (16%) rGO/3D ZnO sample is superior to the other samples, long-term stability tests have been performed on it. After 40 000 cycles, this sample's Coulombic efficiency and specific capacitance retention values were 100%, and the sample managed to maintain its performance without any decrease.

Areal capacitance values of the prepared PSC devices with rGO in the composite as 16% and 32% ratio depending on the applied current density at a 2 V potential range are given in Fig. 6(a). It was observed that the areal capacitance values of the (16%) rGO composite reached the maximum under UV radiation. Notably, the PSC device with (8%) rGO in the composite

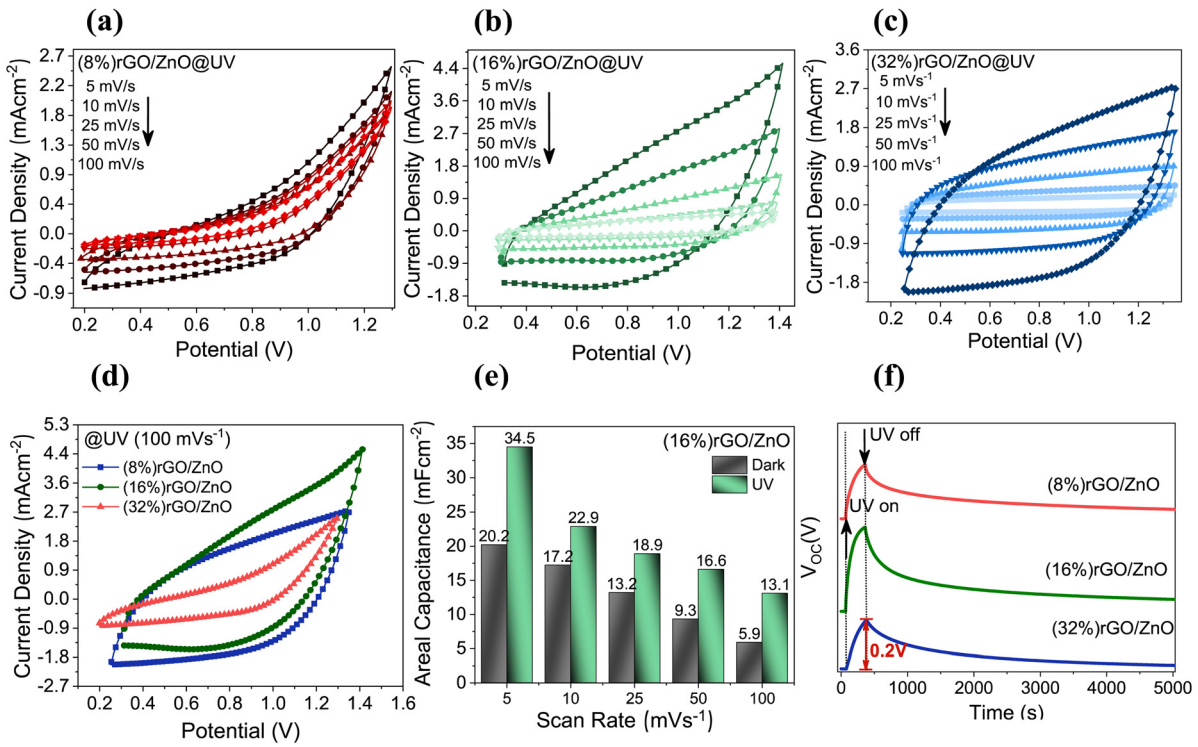

Fig. 4 Electrochemical measurements of the fabricated PSC devices; CV measurements under various scan rates for (a) (8%) rGO/3D ZnO, (b) (16%) rGO/3D ZnO, (c) (32%) rGO/3D ZnO under UV illumination (8.8 mW of power intensity), (d) comparison for CV profiles at a 100 mV s^{-1} of scan rate, (e) areal capacitance comparison under UV illumination and at dark, and (f) changes in open circuit potential with UV on–off cycle.

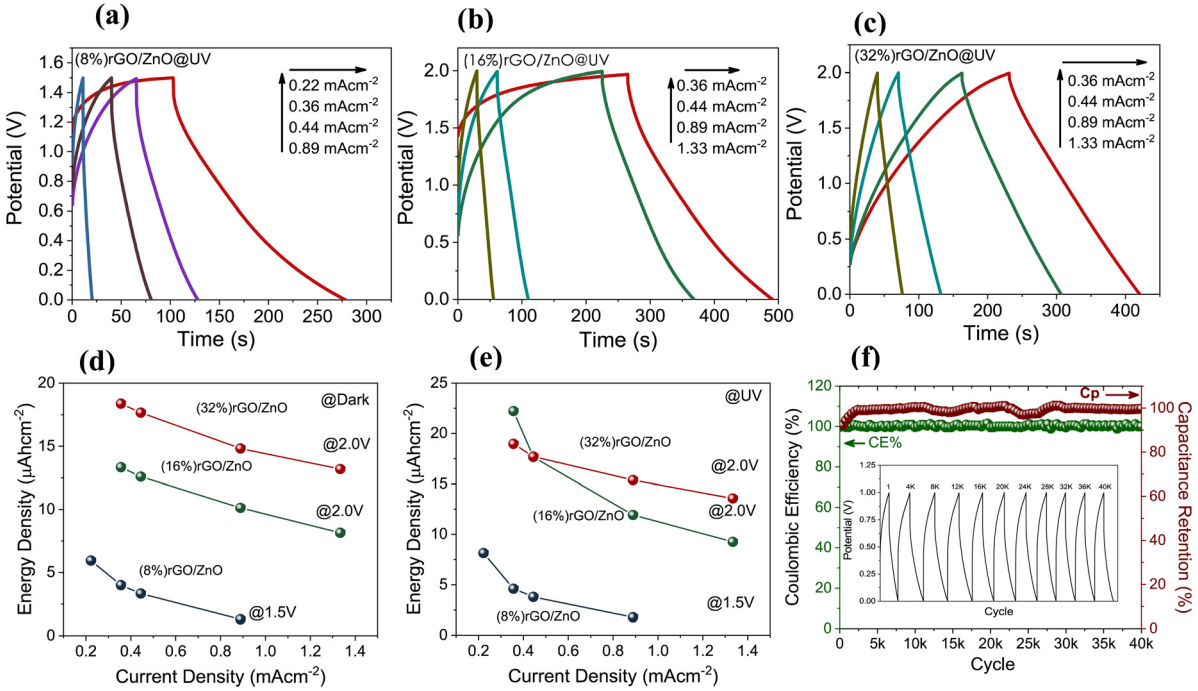

Fig. 5 GCD curves of the (a) (8%) rGO/3D ZnO, (b) (16%) rGO/3D ZnO, and (c) (32%) rGO/3D ZnO under UV illumination (8.8 mW of power intensity), energy density values in the (d) dark and (e) UV illuminated environments, and (f) long term cycling stability of the PSC devices based on the (16%) rGO/3D ZnO composite material with the inset figure displaying the GCD curves at specific cycles.

could reach a maximum of up to 1.5 V potential range under the same applied current densities. Ragone plots are graphs used to understand the performance of energy storage devices and show the change of energy densities according to power

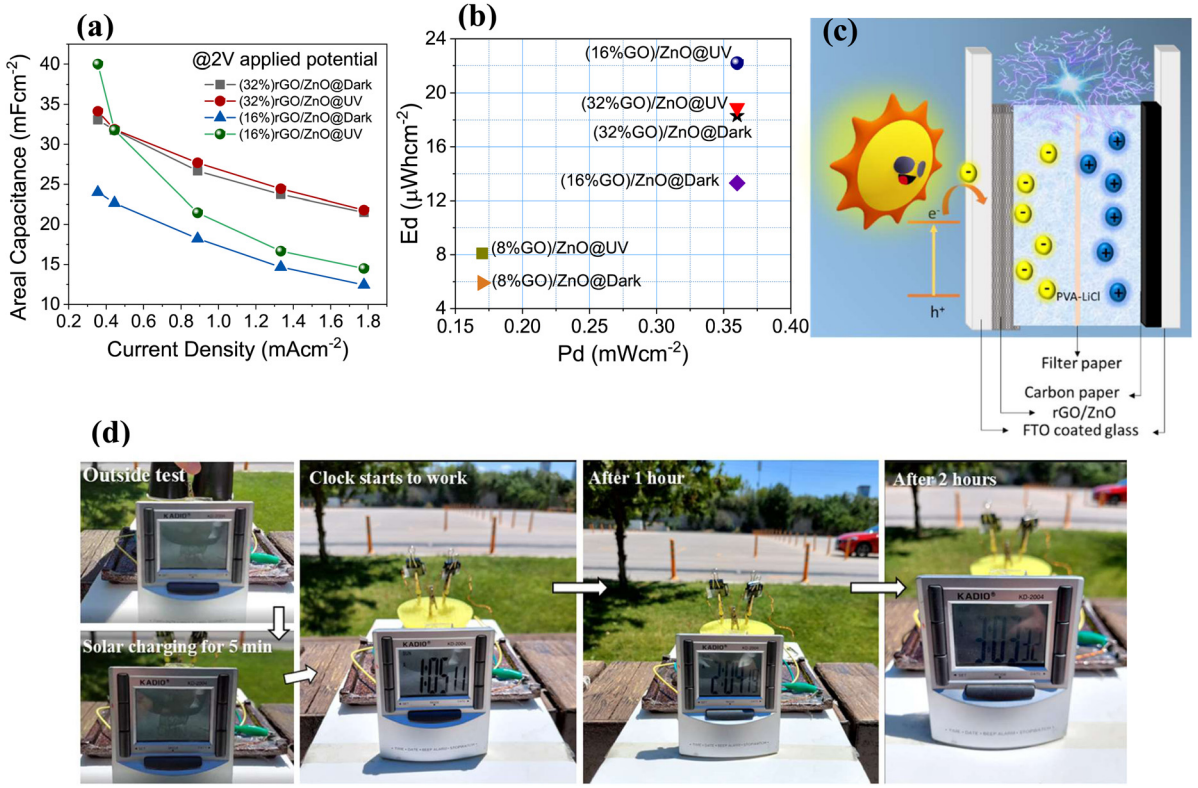

Fig. 6 (a) Comparative areal capacitance values depending on the applied current density at a 2 V potential range, (b) Ragone plot and (c) schematic diagram of the photo charge–discharge step, and (d) pictures taken from the outdoor test.

densities. The biggest disadvantage of SCs is that they have lower energy density than batteries. It was determined that the energy densities of all rGO/3D ZnO-based devices that we developed in this study increased with exposure to UV light (Fig. 6(b)). In addition, as the amount of rGO in the composite increased from 8% to 32%, the energy densities calculated by measuring under dark conditions increased 3 times from 6 μW h cm^{-2} to 18 μW h cm^{-2}, showing that increasing the amount of rGO in the structure increases the amount of charge that can be stored. On the other hand, due to ZnO's superior optical absorption properties under illumination, the 16% rGO-containing device performed best. In other words, 32% of rGO-containing electrodes had similar energy densities in the dark and under illumination. The highest energy and power densities of 22 μW h cm^{-2} and 0.36 mW cm^{-2} have been calculated for the (16%) rGO/3D ZnO-based PSC, respectively, under UV light. When we compare it with PSC devices previously reported in the literature, it can be seen that the performance values we obtained in this study are one of the best (Table 1). In PSC devices with dual-effect electrodes, the photoactive electrode ensures that the charge carriers produced by light are stored on the same electrode. In our study, the rGO/3D ZnO electrode becomes more negatively charged by retaining light-excited electrons (Fig. 6(c)), providing less energy consumption when the device is charged with grid electricity. Solar energy must be used directly to operate completely independently of the grid. In our experiment, to show that the rGO/3D ZnO-based PSC device can operate independently of the grid electricity, we connected two PSC devices in series and used them to power a digital clock. The system was exposed to daylight. After about 5 minutes, the digital clock started working and continued to work for more than 2 hours (see Fig. 6(d)). With this outside experiment, we proved that it is possible to use our system in autonomous devices that meet their power needs.

Electrochemical impedance spectroscopy (EIS) studies, which provide useful information about the electrochemical charge transportation properties, have been performed to investigate further the rGO/ZnO dual-acting electrodes in the dark and under UV illumination (Fig. 7(a) and (b)) in the frequency range of 100 mHz to 100 kHz. All the PSC devices could be modeled with the same equivalent circuit (EC). Each obtained curve indicated a well-defined semicircle in the high-frequency region followed by a tail in the low-frequency region and a clear diminishing in the resistance when the condition changes from dark to UV light.[35] However, the size of the semicircle decreases with increasing rGO contents in the composite owing to the intrinsic high ionic conductivity of rGO fast electron transfers. It is known that the diameter of the semicircle defines the charge-transfer resistance (R_{CT}), coming from the resistance of electrochemical reactions.[75] The real axis intercept defines the contact resistance (R_S) in the high-frequency region. This EC parameter relates to the electrolyte's ionic resistance, the electrode's intrinsic resistance, and the interface resistance between the electrolyte and the working electrode. The slope of the vertical line in the low-frequency region is adversely related to the ion diffusion resistance within the electrodes. Therefore, the observation of more vertical lines for the (32%) rGO/3D ZnO-based PSC device as compared to that with the least rGO content (8%) means that this PSC device exhibited a more enhanced capacitance characteristic, supporting the results obtained from the CV and GCD analysis. Circuit equivalents of these Nyquist graphs and numerical values of the circuit elements are given in the ESI† (Table S2). The modeled EC circuit was also given in Fig. S6 (ESI†). Bode plots of the (16%) rGO/3D ZnO composite-based PSC device were also examined to understand their capacitive behavior in the dark and under UV illumination, respectively (Fig. 7(c) and (d)). As seen in the Bode plot, the decreased $|Z|$ value at the lower frequency suggests the higher conductivity of the PSC device under UV radiation.[76] Bode plots of (8%) rGO/3D ZnO and (32%) rGO/3D ZnO-based PSC devices under UV and in the dark conditions are given in Fig. S7 (ESI†) for comparison.

A proof-of-concept test was conducted to determine the performance of the single PSC device after charging under UV light (Fig. 8). As expected, according to GCD tests, the charge time increases as the charge current density decreases (Fig. 8(a)). It has also been determined that the device can operate efficiently at a high operating potential of 2.2 V. Moreover, upon UV-charging, the (16%) rGO/3D ZnO device holds the charge for a long time (Fig. 8(b)). In other words, after charging up to 2.2 V at 0.88 mA cm^{-2}, an *IR* drop has been observed, resulting in 1.9 V of initial discharge voltage. After 1000 seconds, the voltage was about 1.4 V, and the device held the 1.0 V for more than 5000 seconds. Besides, after charging at 0.88 mA cm^{-2} to 2.2 V, a single PSC device could power a digital clock for about 2 hours under UV illumination (Fig. 8(c)). In

Table 1 A comparison table for performance parameters of the present work with the literature based on solar-assisted supercapacitors

Photo-electrode	Electrolyte	C_A (mF cm^{-2})	J (mA cm^{-2})	E_d (μW h cm^{-2})	P_d (mW cm^{-2})
N_3-dye adsorbed TiO_2[52]	0.5 M LiI/0.05 M I_2/0.5 M TBP in CH_3CN	6.5	NA	0.0213	0.6
GO-PEDOT:PSS[16]	PVA/H_3PO_4	6.12	0.005	0.71	0.05
ZnO/$ZnCo_2O_4$[68]	PVA/KOH	0.15	1.2×10^{-3}	11.6×10^{-3}	NA
CF-MoS_2[69]	PVA/H_2SO_4	7.00	0.01	NA	NA
Hematite/$Ni(OH)_2$/Prussian white[70]	1 M KCl	2.16	0.12	NA	NA
$MAIBiI_3$[71]	PVA/CB-H_3PO_4	4.00	0.01	0.55	7.5
$BiVO_4$−PbO_x[72]	0.1 M phosphate buffer	6.0	0.015	NA	NA
$Ni(OH)_2$/TiO_2[73]	1 M NaOH	22.9	0.05	NA	NA
TiO_2/$CsPbBr_3$/C[74]	Silica gel/H_3PO_4	33.8	0.375	6.8	0.45
rGO/3D ZnO (this work)	PVA/LiCl	40.00	0.4	22	0.36

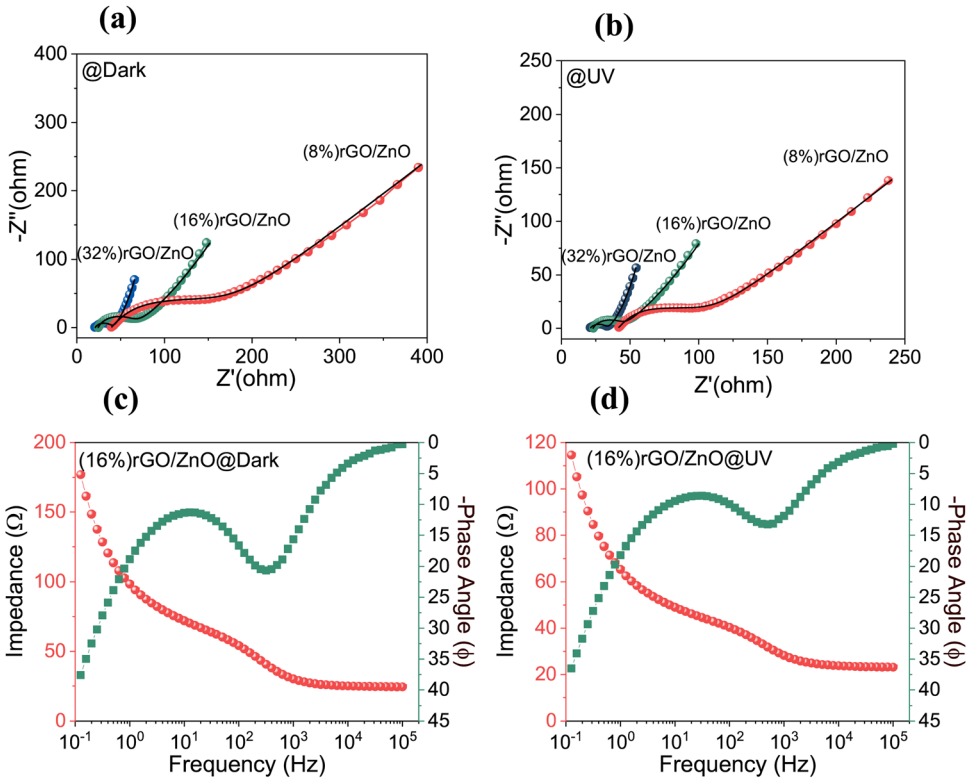

Fig. 7 Nyquist plots of rGO/3D ZnO photoelectrodes (a) in the dark and (b) under UV illumination, Bode plots of the (16%) rGO/3D ZnO based PSC device (c) in the dark and (d) under UV light.

addition, Fig. S8 (ESI†) shows GCD curves at various current densities under AM1.5 simulated solar irradiation, photo charging, self-discharge processes, and the related proof of concept photographs. The self-discharge time was observed to

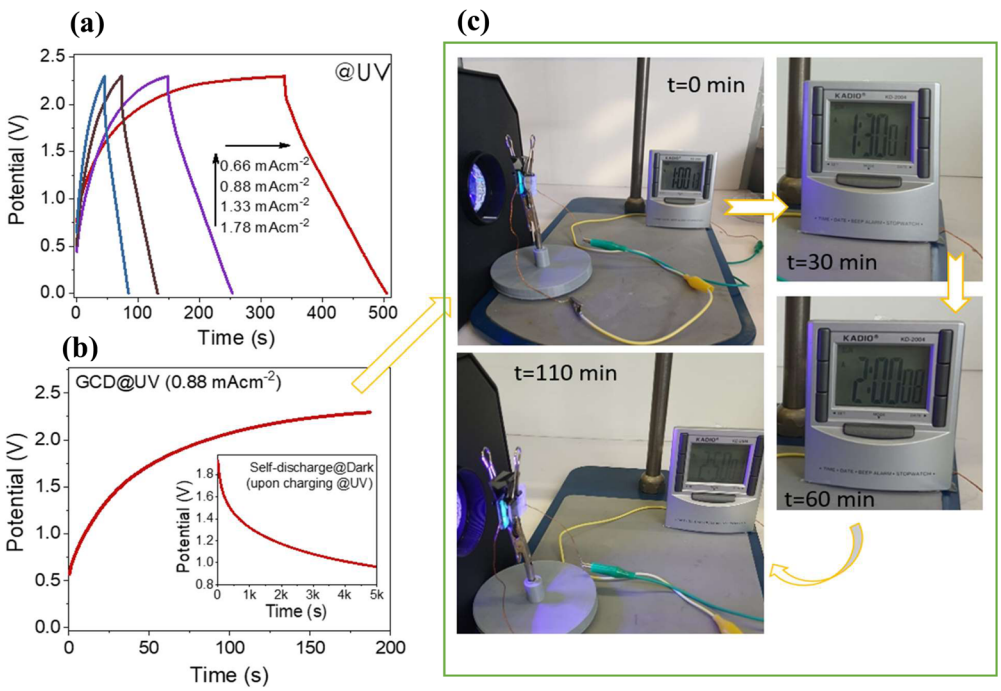

Fig. 8 Proof of concept experiments: (a) GCD curves at 2.2 V under UV illumination, (b) charging at a 0.88 mA cm^{-2} current density, and (c) photographic images of the PSC device for powering a digital watch after charging under UV illumination.

be more than 5000 s to decrease to 1.1 V (well enough to power the digital clock) after photocharging under solar irradiation at 0.2 A g^{-1} (0.9 mA cm^{-2}) up to 2.2 V.

Conclusions

In conclusion, in this work, we presented that reduced graphene oxide (rGO) and zinc oxide nanoflake (ZnO) structures have been successfully combined to produce dual-acting electrodes for photo-supercapacitor devices. To better understand the effect of rGO and ZnO separately, three different compositions have been studied, in which the weight percent of rGO changes from 8 to 32%. SEM and TEM analysis showed that when the rGO percent increased, ZnO nanoflakes dispersed better in the composites. Raman analysis revealed that as the percentage increased in the composites, characteristic structural peaks of rGO became more dominant. All samples presented strong optical absorption in the UV region. Besides, *via* increasing the rGO, an optical shift through the visible range has been observed. Combined with the PL measurements, it can be concluded that the decrease in UV emissions and an increase in blue emissions by varying the composite ratio can be attributed to anchoring the rGO sheets on the ZnO surface.

Furthermore, the ZnO-related EPR signals start to vanish when increasing the rGO content, indicating that the defect centers present in the pristine ZnO material play a key role in forming the composite materials. When the results of EIS measurements were examined, it was seen that with the addition of rGO, the composites' bulk and interfacial layer resistances decreased, but the charge transfer resistances increased. UV illumination resulted in a further decrease in bulk and interfacial layer resistances compared to the dark condition. On the other hand, charge transfer resistance increased drastically under UV, probably due to the high capacitive effect of the (16%) rGO/ZnO-based PSC. It has been observed that the device performance varies depending on the amount of rGO in the structure so that the CV and GCD measurements coincide with the information obtained from the material properties. Generally, as the amount of rGO increases, the energy density increases, but above a critical value, the composite material begins to lose its light sensitivity. Therefore, the electrodes containing 16% rGO performed better than those containing 32% and 8%. As a result, the (16%) rGO/ZnO-based PSC exhibited superior performance compared to other samples, with its ability to maintain 100% of its performance at 40 000 cycles, its areal capacitance of 40 mF cm^{-2} and energy density values of 22 μW h cm^{-2}. The devices we produce seem to have great potential for use in portable systems that meet their own power needs in the future due to their advantages, such as working in sunlight and the device design being simple and suitable for mass production.

Author contributions

C. T. A. and T. O. C. performed the fabrication and characterization of the samples. C. T. A. also contributed to the data analysis and preparation of the manuscript. A. M. R., M. H. A., I. D. Y., and E. E. performed the electron paramagnetic resonance measurements and data analysis. L. B. T. performed the SEM and TEM analysis. E. E. and F. B. M. performed PL and Raman analysis and interpreted the data. C. S. and M. D. L. synthesized the reduced graphene oxide powders. N. D. S. and M. S. are the primary investigators of the study. N. D. S. and M. S. performed the data analysis and wrote the manuscript. All authors reviewed and commented on the manuscript at all stages.

Data availability

Data will be made available on request.

Conflicts of interest

The authors declare that they have no known competing financial interests or personal relationships that could have appeared to influence the work reported in this paper.

Acknowledgements

N. D. S. and M. S. would like to acknowledge the partial financial support of TUBITAK under the research contract 122F390. A. M. R. acknowledges the partial financial support from the Romanian Ministry of Research, Innovation and Digitalization, Nucleu Program within the National Research Development and Innovation Plan 2022-202, project number PN 23 24 01 03.

References

1 M. S. Zantye, A. Gandhi, Y. Wang, S. P. Vudata, D. Bhattacharyya and M. M. F. Hasan, *Energy Environ. Sci.*, 2022, **15**, 4119–4136.
2 S. S. Mani, S. Rajendran, P. S. Arun, A. Vijaykumar, T. Mathew and C. S. Gopinath, *Energy Adv.*, 2024, **3**, 829–840.
3 A. Ravilla, C. A. R. Perini, J.-P. Correa-Baena, A. W. Y. Ho-Baillie and I. Celik, *Energy Adv.*, 2024, **3**, 800–811.
4 V. Rathi, R. Brajpuriya, R. Gupta, K. P. S. Parmar and A. Kumar, *Energy Adv.*, 2024, **3**, 389–412.
5 N. Chepngetich, G. M. Mumbi, G. Meheretu, K. K. Richard, G. K. Yegon, S. C. Chepkwony, C. K. Rono, D. Sanni, A. Bello and E. Ntsoenzok, *Energy Adv.*, 2024, **3**, 741–764.
6 *Solar Fuels*, ed N. D. Sankir and M. Sankir, Wiley, Scrivener Publishing, 2023, pp. 285–339, ISBN:9781119752097.
7 A. Kumtepe, C. T. Altaf, N. S. Sahsuvar, N. Abdullayeva, E. Koseoglu, M. Sankir and N. D. Sankir, *ACS Appl. Energy Mater.*, 2020, **3**, 3127–3133.
8 C. T. Altaf, M. Sankir and N. Demirci Sankir, *Mater. Lett.*, 2021, **304**, 130602.
9 C. T. Altaf, N. S. Sahsuvar, N. Abdullayeva, O. Coskun, A. Kumtepe, E. Karagoz, M. Sankir and N. Demirci Sankir, *ACS Sustainable Chem. Eng.*, 2020, **8**, 15209–15222.

10 R. Leil, M. M. Abodouh, N. Javed, S. Sreekumar, H. Pacheco, N. Tarek, D. M. O'Carroll and N. K. Allam, *Energy Adv.*, 2024, **3**, 430–441.
11 *Hydrogen Storage Technologies*, ed N. D. Sankir and M. Sankir, Wiley, Scrivener Publishing, 2018.
12 S. Chu, X. Wang, L. Yang, H. Zhang, R. Xiao, Y. Wang and Z. Zou, *Energy Adv.*, 2023, **2**, 556–564.
13 C. T. Altaf, N. Abdullayeva and N. D. Sankir, *Photoelectrochem. Sol. Cells*, 2018, 251–303.
14 R. Leil, M. M. Abodouh, N. Javed, S. Sreekumar, H. Pacheco, N. Tarek, D. M. O'Carroll and N. K. Allam, *Energy Adv.*, 2024, **3**, 430–441.
15 N. Flores-Diaz, F. De Rossi, A. Das, M. Deepa, F. Brunetti and M. Freitag, *Chem. Rev.*, 2023, **123**, 9327–9355.
16 D. C. T. Nguyen, V.-D. Mai, V.-P. Vu, S. Kim and S.-H. Lee, *J. Power Sources*, 2023, **572**, 233086.
17 C. Tuc Altaf, A. M. Rostas, A. Popa, D. Toloman, M. Stefan, N. Demirci Sankir and M. Sankir, *ACS Omega*, 2023, **8**, 47393–47411.
18 K. Namsheer and C. S. Rout, *J. Mater. Chem. A*, 2021, **9**, 8248–8278.
19 Y. Zhou, H. Qi, J. Yang, Z. Bo, F. Huang, M. S. Islam, X. Lu, L. Dai, R. Amal, C. H. Wang and Z. Han, *Energy Environ. Sci.*, 2021, **14**, 1854–1896.
20 Y. Zhao, H. Li, R. Tang, X. Wang, Y. Wu, S. Yan and Y. Zhang, *J. Mater. Chem. A*, 2023, **11**, 15844–15854.
21 T. Zhu, Z. He, Z. An, R. Xu, Y. Li, R. Zhe, H.-E. Wang and H. Pang, *Sci. China Mater.*, 2023, **66**, 2216–2226.
22 T. Zhu, J. Pan, Z. An, R. Zhe, Q. Ou and H.-E. Wang, *J. Mater. Chem. A*, 2022, **10**, 20375–20385.
23 W. J. Dong, W. S. Cho and J.-L. Lee, *ACS Appl. Mater. Interfaces*, 2021, **13**, 22676–22683.
24 K. Namsheer and C. S. Rout, *J. Mater. Chem. A*, 2021, **9**, 8248–8278.
25 D. Devadiga, M. Selvakumar, P. Shetty and M. S. Santosh, *Renewable Sustainable Energy Rev.*, 2022, **159**, 112252.
26 T. Berestok, C. Diestel, N. Ortlieb, J. Buettner, J. Matthews, P. S. C. Schulze, J. C. Goldschmidt, S. W. Glunz and A. Fischer, *Sol. RRL*, 2021, **5**, 1–13.
27 F. Zhou, Z. Ren, Y. Zhao, X. Shen, A. Wang, Y. Y. Li, C. Surya and Y. Chai, *ACS Nano*, 2016, **10**, 5900–5908.
28 D. Wang, C. Wang, F. P. García de Arquer, J. Zhong, L. Qian, L. Fang, P. Liu, Y. Pang, M. M. Liu, M. M. Liu, G. Zheng, D. Sinton, E. H. Sargent, H. Yang and B. Zhang, *J. Mater. Chem. A*, 2017, **5**, 3167–3171.
29 T. O. Colak, C. T. Altaf, F. N. T. Yesilbag, Y. O. Yesilbag, I. D. Yildirim, E. Erdem, F. B. Misirlioglu, N. D. Sankir and M. Sankir, *J. Energy Storage*, 2024, **86**, 111274.
30 C. T. Altaf, D. Yolacan and N. D. Sankir, *Mater. Lett.*, 2019, **236**, 710–714.
31 C. T. Altaf, N. Abdullayeva, O. Coskun, A. Kumtepe, I. D. Yildirim, E. Erdem, M. Liu, A. Bozbey, E. Agar, M. Sankir and N. D. Sankir, *Phys. Rev. Mater.*, 2021, **125403**, 1–14.
32 I. Shaheen, K. S. Ahmad, C. Zequine, R. K. Gupta, A. G. Thomas and M. A. Malik, *RSC Adv.*, 2021, **11**, 23374–23384.
33 D. Solís-Cortés, E. Navarrete-Astorga, R. Schrebler, J. J. Peinado-Pérez, F. Martín, J. R. Ramos-Barrado and E. A. Dalchiele, *RSC Adv.*, 2020, **10**, 5712–5721.
34 C. T. Altaf, O. Coskun, A. Kumtepe, A. M. Rostas, I. Iatsunskyi, E. Coy, E. Erdem, M. Sankir and N. D. Sankir, *Sci. Rep.*, 2022, **12**, 11487.
35 C. T. Altaf, T. O. Colak, A. M. Rostas, M. Mihet, M. D. Lazar, I. Iatsunskyi, E. Coy, I. D. Yildirim, F. B. Misirlioglu, E. Erdem, M. Sankir and N. D. Sankir, *J. Energy Storage*, 2023, **68**, 107694.
36 C. T. Altaf, T. O. Colak, E. Erdem, U. Unal, F. B. Misirlioglu, G. G. Condorelli, N. D. Sankir and M. Sankir, *Electrochim. Acta*, 2023, **456**, 142415.
37 C. T. Altaf, T. O. Colak, F. Lufrano, G. S. Unal, N. D. Sankir and M. Sankir, *J. Energy Storage*, 2022, **55**, 105784.
38 T. O. Colak, C. T. Altaf, F. N. T. Yesilbag, Y. O. Yesilbag, I. D. Yildirim, E. Erdem, F. B. Misirlioglu, N. D. Sankir and M. Sankir, *J. Energy Storage*, 2024, **86**, 111274.
39 C. T. Altaf, A. M. Rostas, M. Mihet, M. D. Lazar, I. Iatsunskyi, E. Coy, E. Erdem, M. Sankir and N. D. Sankir, *J. Mater. Chem. C*, 2022, **10**, 10748–10758.
40 C. Tuc Altaf, T. O. Colak, A. M. Rostas, A. Popa, D. Toloman, M. Suciu, N. Demirci Sankir and M. Sankir, *ACS Omega*, 2023, **8**, 14952–14964.
41 N. Abdullayeva, C. Tuc Altaf, A. Kumtepe, N. Yilmaz, O. Coskun, M. Sankir, H. Kurt, C. Celebi, A. Yanilmaz and N. Demirci Sankir, *ACS Appl. Nano Mater.*, 2020, **3**, 5881–5897.
42 O. Coskun, C. T. Altaf, M. Sankir and N. D. Sankir, *Mater. Lett.*, 2022, **325**, 132900.
43 N. A. Eroglu, T. C. Altaf, D. N. Sankir and M. Sankir, *Opt. Mater.*, 2024, **148**, 114763.
44 S. Nadupalli, S. Repp, S. Weber and E. Erdem, *Nanoscale*, 2021, **13**, 9160–9171.
45 S. Bai, N. Zhang, C. Gao and Y. Xiong, *Nano Energy*, 2018, **53**, 296–336.
46 J. Liang, G. Zhu, C. Wang, Y. Wang, H. Zhu, Y. Hu, H. Lv, R. Chen, L. Ma, T. Chen, Z. Jin and J. Liu, *Adv. Energy Mater.*, 2017, **7**, 1601208.
47 X. Zhou, X. Yue, Y. Dong, Q. Zheng, D. Lin, X. Du and G. Qu, *J. Colloid Interface Sci.*, 2021, **599**, 68–78.
48 S. Kasap, I. I. Kaya, S. Repp and E. Erdem, *Nanoscale Adv.*, 2019, **1**, 2586–2597.
49 M. Buldu-Akturk, M. Toufani, A. Tufani and E. Erdem, *Nanoscale*, 2022, 3269–3278.
50 C. V. Pham, S. Repp, R. Thomann, M. Krueger, S. Weber and E. Erdem, *Nanoscale*, 2016, **8**, 9682–9687.
51 A. A. Yaqoob, N. H. Mohd Noor, A. Serrà and M. N. Mohamad Ibrahim, *Nanomaterials*, 2020, 10.
52 C.-Y. Hsu, H.-W. Chen, K.-M. Lee, C.-W. Hu and K.-C. Ho, *J. Power Sources*, 2010, **195**, 6232–6238.
53 S. Nandi, S. Kumar and A. Misra, *Mater. Adv.*, 2021, **2**, 6768–6799.
54 A. Das, M. Ojha, P. Subramanyam and M. Deepa, *Nanoscale Adv.*, 2020, **2**, 2925–2942.
55 A. Roy, P. Majumdar, P. Sengupta, S. Kundu, S. Shinde, A. Jha, K. Pramanik and H. Saha, *Electrochim. Acta*, 2020, **329**, 135170.

56 O. Usman, M. Ikram, N. Abid, M. Saeed, A. Bashir, W. Nabgan, N. Mushahid and M. Ikram, *ACS Omega*, 2022, **7**, 26715–26722.
57 M. Schumm, PhD dissertation, Julius Maximilian University of Würzburg, 2008, pp. 21–23.
58 M. Toufani, S. Kasap, A. Tufani, F. Bakan, S. Weber and E. Erdem, *Nanoscale*, 2020, **12**, 12790–12800.
59 Q.-P. Luo, X.-Y. Yu, B.-X. Lei, H.-Y. Chen, D.-B. Kuang and C.-Y. Su, *J. Phys. Chem. C*, 2012, **116**, 8111–8117.
60 S. Palsaniya, H. B. Nemade and A. K. Dasmahapatra, *J. Phys. Chem. Solids*, 2021, **154**, 110081.
61 S. Abdolhosseinzadeh, H. Asgharzadeh, S. Sadighikia and A. Khataee, *Res. Chem. Intermed.*, 2016, **42**, 4479–4496.
62 J. Shah, A. Shukla, M. Kar, G. Gupta, S. Jain and R. K. Kotnala, *React. Chem. Eng.*, 2022, **7**, 1836–1846.
63 L. Kumar Jangir, Y. Kumari, A. Kumar, M. Kumar and K. Awasthi, *Mater. Chem. Front.*, 2017, **1**, 1413–1421.
64 N. Abdullayeva, C. T. Altaf, M. Mintas, A. Ozer, M. Sankir, H. Kurt and N. D. Sankir, *Sci. Rep.*, 2019, **9**, 1–14.
65 A. U. Ammar, I. D. Yildirim, M. H. Aleinawi, M. Buldu-Akturk, N. S. Turhan, S. Nadupalli, A. M. Rostas and E. Erdem, *Mater. Res. Bull.*, 2023, **160**, 112117.
66 M. H. Aleinawi, A. U. Ammar, M. Buldu-Akturk, N. S. Turhan, S. Nadupalli and E. Erdem, *J. Phys. Chem. C*, 2022, **126**, 4229–4240.
67 P. Jakes and E. Erdem, *Phys. Status Solidi RRL*, 2011, **5**, 56–58.
68 B. D. Boruah and A. Misra, *ACS Appl. Energy Mater.*, 2019, **2**, 278–286.
69 S. Kumar, A. Mukherjee, S. Telpande, A. Das Mahapatra, P. Kumar and A. Misra, *J. Mater. Chem. A*, 2023, **11**, 4963–4976.
70 M. Mohammadian, S. Rashid-Nadimi and Z. Peimanifard, *J. Power Sources*, 2019, **426**, 40–46.
71 I. K. Popoola, M. A. Gondal, A. Popoola and L. E. Oloore, *J. Energy Storage*, 2022, **53**, 105167.
72 S. Safshekan, I. Herraiz-Cardona, D. Cardenas-Morcoso, R. Ojani, M. Haro and S. Gimenez, *ACS Energy Lett.*, 2017, **2**, 469–475.
73 P. Chen, C. Cao, C. Ding, Z. Yin, S. Qi, J. Guo, M. Zhang and Z. Sun, *J. Power Sources*, 2022, **521**, 230920.
74 J. Liang, G. Zhu, C. Wang, P. Zhao, Y. Wang, Y. Hu, L. Ma, Z. Tie, J. Liu and Z. Jin, *Nano Energy*, 2018, **52**, 239–245.
75 C. He, S. Qiu, S. Sun, Q. Zhang, G. Lin, S. Lei, X. Han and Y. Yang, *Energy Environ. Mater.*, 2018, **1**, 88–95.
76 M. Chandel, P. Makkar and N. N. Ghosh, *ACS Appl. Electron. Mater.*, 2019, **1**, 1215–1224.